



Article

Influence of the Friction Coefficient on the Stress Distributions and Contact Pressure in Press-Fits via Finite Element Analysis

Eulalia Izard ¹, Roberto Garcia-Martín ² , Manuel Rodríguez-Martín ² and Miguel Lorenzo ^{2,*}

¹ Department of Mechanical Engineering, University of Salamanca, ETSII, Avda. Fernando Ballesteros, 2, 37700 Béjar, Spain; eia@usal.es

² Department of Mechanical Engineering, University of Salamanca, EPS de Zamora, Avda. Cardenal Cisneros, 34, 49029 Zamora, Spain; toles@usal.es (R.G.-M.); ingmanuel@usal.es (M.R.-M.)

* Correspondence: mlorenzo@usal.es; Tel.: +34-677-552-423

Abstract: Press fits are a simple and effective method for assembling a shaft into a hub for different applications in the mechanical engineering field. This method consists of forcing to pass a shaft into a hub via axial insertion. As a result of the difference in the diameters of both components of the shaft and hub, a radial interference is generated, causing a contact pressure at the interface shaft–hub. Contact pressure and the friction coefficient are key factors influencing the maximum transmitted torque. So, in this study, different scenarios for the assembly of a press fit were simulated using finite elements (FE) in order to reveal the influence of this key parameter on the manufacturing-induced stresses in the hub. This way, different friction conditions were considered in terms of the friction coefficient from the frictionless case to a case of high dry friction. In addition, different hub geometries were analyzed including conventional hubs and chamfer hubs with optimal geometry that allows lowering the localized stress concentrations at the hub edges. This way, a more realistic estimation of the final stress state of a press fit is obtained. According to the obtained results, the friction coefficient is revealed as a key parameter in the resulting stress field, causing a non-uniform distribution of stress that can affect the mechanical performance of the press-fit assembly.

Keywords: press fit; friction; chamfer hub; stress reduction; stress concentration; contact pressure



Citation: Izard, E.; Garcia-Martín, R.; Rodríguez-Martín, M.; Lorenzo, M. Influence of the Friction Coefficient on the Stress Distributions and Contact Pressure in Press-Fits via Finite Element Analysis. *Lubricants* **2023**, *11*, 472. <https://doi.org/10.3390/lubricants11110472>

Received: 4 September 2023

Revised: 24 October 2023

Accepted: 30 October 2023

Published: 3 November 2023



Copyright: © 2023 by the authors. Licensee MDPI, Basel, Switzerland. This article is an open access article distributed under the terms and conditions of the Creative Commons Attribution (CC BY) license (<https://creativecommons.org/licenses/by/4.0/>).

1. Introduction

Press fits are a simple and widely used method for assembling a shaft into a hub for diverse mechanical engineering applications. Hub is a general term that represents many different machine components such as gears, bearings, pulleys, cams, wheels, etc. [1–4]. Briefly, this method consists of forcing to pass a shaft into a hub (the radial dimension of both components must be different) by applying an axial force to the shaft [5]. The required force for assembling a press fit depends on the resulting contact pressure and on the friction coefficient existing between both components [6,7]. Friction is dependent on the nature of materials, surface roughness, lubrication, etc. [8–11]. Friction also influences the maximum transmitted torque of the press fit [1,6,7].

As a result of the difference in the diameters of both the shaft and hub, a radial interference is generated in the shaft–hub assembly, causing a contact pressure at the interface hub–shaft. The equations used for the design of these components are obtained from the theory of elasticity by considering both the shaft and hub with the same length. These equations estimate a uniformly distributed contact pressure at the interface hub–shaft [6,7]. However, in mechanical engineering applications, the shaft is commonly longer than the hub and, as a consequence, a local stress concentration unpredicted by theory appears at the hub edges [12–14]. These stress concentrations affect the mechanical performance of the assembly. In addition, the design equations do not take into account the plastic strains that appear after the insertion of the shaft into the hub [15,16]. The presence of plastic strains at the shaft–hub interface is a non-desirable scenario since plastic strains can affect

the adequate performance of the joint, causing zones at the interface shaft–hub without contact, i.e., without contact pressure and vibrations that can produce fretting fatigue, the most common cause of failure of this type of assemblies [17–19], or fretting wear [20–22], causing crack initiation [23].

This way, the assembly process causes a non-uniform contact pressure at the interface shaft–hub that is quite different to the uniform contact pressure given via the theory of pressure cylinder used for designing the press fits. There are different methods used for reducing such stress concentrations that consists of modifying the geometry of the hub [24–29]: the use of round grooved hubs [24,25], the chamfer hubs [26,27], or the use of contact pressure rings [28]. More complex hub geometries are considered in [16] where a hub with an exponential variated thickness in the radial direction was considered. Furthermore, other studies are focused on the analysis of hubs with a variable radial interference [27] or functionally graded materials [14,29]. The experimental determination of contact pressure at the hub–shaft interface exhibits serious difficulties. In many studies [30–32], numerical simulations via the finite element method (FEM) are used as an alternative method for quantitatively estimating the contact pressure.

The use of stress relieving hub geometries causes a reduction in the contact pressure of the assembly and, hence, a reduction in the maximum transmitted torque. So, the optimal design is the one that reduces the stress concentration without causing a significant loss of maximum transmitted torque and contact pressure.

Taking into account the key role of friction on the performance of a press fit, it is interesting to study the influence of the friction coefficient on the stress distributions after the assembly of a press fit for diverse friction conditions. This way, a more realistic estimation of the contact pressure in conventional and optimized chamfer hub geometries can be used for the design of press fits considering the manufacturing effects on the stress states. So, within this framework, this study tries to quantify, by means of numerical simulations using FEM, the contact pressure distributions after the manufacturing of a press fit, including the plasticity effects and the non-uniform distributions unpredicted by theory in conventional and optimized chamfer hubs. Thus, the loss of transmitted torque can be estimated and considered for selecting the optimal geometry by taking into account the induced manufacturing effects on contact pressure. Thus, to achieve this goal, in this study different scenarios for the press-fit assembly were simulated using finite elements (FE) in order to reveal the role of the friction coefficient in the manufacturing-induced stress in the shaft–hub assembly by considering different friction conditions, hub geometries (conventional hubs and optimal chamfer hubs), hub thicknesses, and radial interferences.

2. Materials and Methods

The theory of thick-walled pressure cylinders [6,7] was used to obtain the design equations for estimating the contact pressure p in interference fits under the assumption that both the shaft and hub are made of the same material as follows:

$$p = \frac{E \delta}{2R} \left(1 - \frac{R^2}{r_o^2} \right) \quad (1)$$

where E is the Young's modulus, δ is the radial interference, R is the radius at the shaft–hub interface, and r_o is the outer radius of the hub.

As a result of the applied contact pressure, a stress field is generated in both the shaft and hub. The theory establishes that the magnitude of radial stress is equal to contact pressure but opposite in sign, the axial stress value is negligible, and finally, the tangential stress is influenced by contact pressure, p , and the radial dimensions of both the hub and shaft as follows [9,10]:

$$\sigma_{r,o} = -p \quad (2)$$

$$\sigma_{t,o} = \frac{p R^2}{r_o^2 - R^2} \left(1 + \frac{r_o^2}{R^2} \right) \quad (3)$$

To obtain the aforementioned equations, two assumptions were considered: (i) the length of both the hub and shaft is the same and (ii) the hypothesis of the plane strain case of the theory of elasticity are fulfilled. The maximum transmitted torque, T , can be obtained as a function of contact pressure, friction coefficient, μ , and hub geometry as follows [6,7]:

$$T = 2\pi R^2 \mu L p \quad (4)$$

Finite Element Numerical Modeling

The ISO Standard for fits and tolerances establishes the hard press type H7s6 as a suitable interference fit for applications where both transmitting torque and rotation movement of both the shaft and hub are required [33]. In this study, the dimensions of the hub and shaft (Figure 1) were chosen according to previous studies [24] considering the hub length, L , equal to the shaft diameter, d , hence $L/d = 1$ and the shaft length is two times longer than the hub length, $l/L = 2$. Accordingly, the reference case consists of (i) a solid shaft with the following dimensions: $R = 20$ mm and $l = 80$ mm, and (ii) a hollow cylinder (hub) of length $L = 40$ mm and an outer radius $r_o = 40$ mm. Therefore, considering the tolerances of the chosen interference fit 40H7s6, the maximum radial interference is obtained as $\delta = 29.5$ μm . The hub thickness, t , was analyzed in terms of the ratio between the hub thickness and the shaft diameter: $\gamma = t/d$. In this way, the following values of γ were selected in this study: (i) $\gamma = 1/4$, (ii) $\gamma = 3/8$, (iii) $\gamma = 1/2$ (iv) $\gamma = 3/4$, and (v) $\gamma = 1$; hence, for this case, the hub thickness and the shaft diameter are the same.

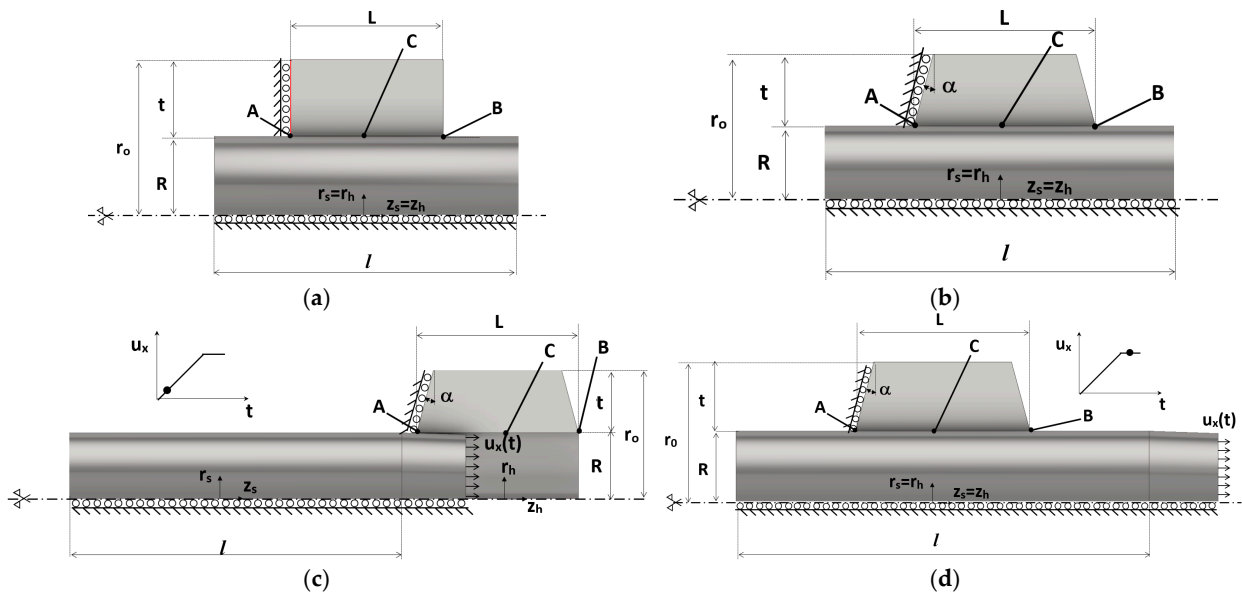


Figure 1. Scheme of two-dimensional finite element modeling of the interference fit: (a) static case for conventional hub, (b) static case for chamfer hub, (c) dynamic simulation at the initial instant, and (d) dynamic simulation at the final instant with both components assembled.

Chamfer hubs (Figure 1b) are a simple geometrical variation in a conventional hub (Figure 1a) that can be defined by just using the chamfer angle, α , (Figure 1b). In this way, the chamfer angle is obtained in terms of the chamfer axial length, l_z , and the hub thickness, t , as $\alpha = \text{atan}(l_z/t)$. Thus, the maximum chamfer angle is obtained when l_z is equal to half of the interface length as follows: $\alpha_{\text{max}} = \text{atan}(L/2t)$. In the present analysis, diverse chamfer angles were considered from $\alpha = 0^\circ$ (conventional hub) up to $\alpha = 20^\circ$ as follows: $\alpha = 0^\circ$, $\alpha = 5^\circ$, $\alpha = 10^\circ$, $\alpha = 15^\circ$, and $\alpha = 20^\circ$. From a technical point of view, the hub width at the upper surface is not wide enough to be used for chamfer angles higher than 20° ; hence, these cases are not considered. All the cases of study considered the same contact hub length, L ; hence, the variations in the maximum transmitted torque are linked to changes in the contact pressure (see Equation (4)).

A common AISI 1020 steel was considered in the simulations for both the shaft and hub with the following material properties: Young's modulus, $E = 186$ GPa; Poisson coefficient, $\nu = 0.29$; and yield strength, $\sigma_Y = 330$ MPa. The constitutive model was considered as having perfectly plastic behavior and the J2 yield criterion was included in the computations.

The revolute symmetry of the shaft–hub assembly (Figure 1) is considered for reducing the FE model to an axisymmetric case (Figure 2) and saves in computing time as a result. In this way, the following boundary conditions were considered: (i) null displacements in the radial direction ($r = 0$) were imposed in the nodes placed at the shaft axis, and (ii) null displacements in the axial direction ($z = 0$) of the nodes of the hub placed at the hub edge at the insertion side (Figure 2).

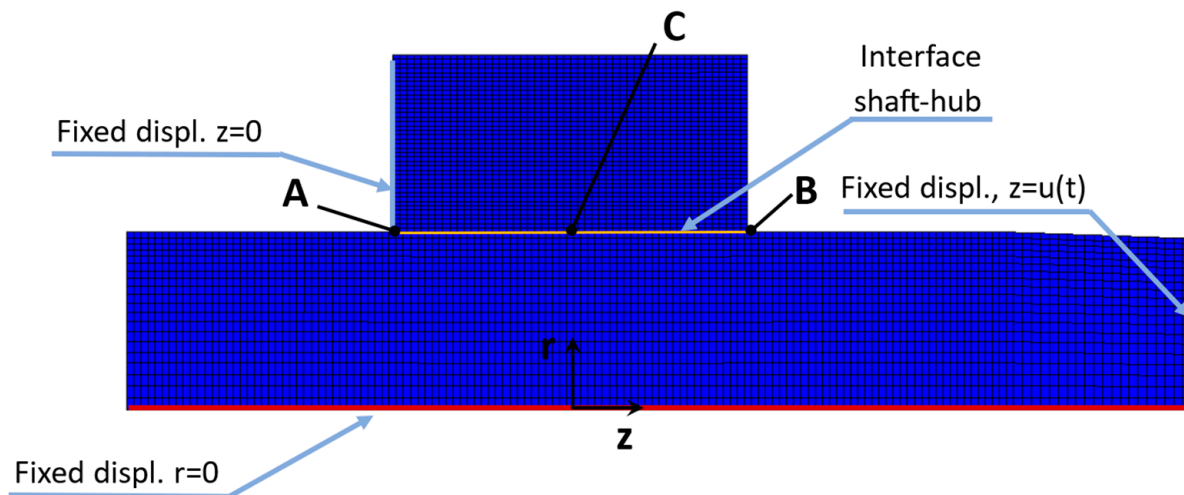


Figure 2. Mesh used in FE calculations identifying the boundary conditions applied.

Two different types of numerical simulation were considered. On one hand, in the static case, both components of the shaft and hub are assembled (Figure 1a,b) and the radial interference was included in the simulations using a built-in function available in the commercial FE code used in this study (MSC.Marc). This way, a certain radial interference that causes a contact pressure at the interface of the hub–shaft assembly is included in the FE simulations. On the other hand, the dynamic case considers the real dimensions of the hub and the shaft and the assembly process of the press fit is simulated, forcing to pass the hub of a higher diameter into the hub of a lower diameter up to reach the final assembly position (Figure 1c,d). This way, a constantly growing displacement ($u(t)$ in Figures 1 and 2) is imposed to the nodes placed at the insertion edge of the shaft (Figure 2) up to reach a value of displacement high enough for placing the shaft at the middle of the hub length. Later, the applied displacement is constant in order to obtain a stable value of the stress distribution at the end of the process. To make the shaft entry within the hub easier, a cone is added to the insertion side of the hub with a conicity of 7% or, in other words, the cone semi-angle is 2° (Figure 1c,d). Contact was selected as a Coulomb-type friction with a given friction coefficient included in the simulations. The value of this parameter was varied to find out the influence on the stress state at the interface as will be discussed later.

A non-uniform mesh of four-node quadrilateral elements was considered for both bodies (shaft and hub) as shown in Figure 2. This way, the element size is increased from the shaft axis to the zone of analysis, the shaft–hub interface. As a result, a finer mesh is placed at the interface with a significant reduction in the computing time.

The required convergence in the results was obtained by considering different meshes according to the mesh factor K_m , defined as the ratio of the number of mesh elements and the number of elements of the base mesh. Thus, different meshes were applied considering a lower size of elements as the mesh factor (K_m) is increased according to the following

sequence: $K_m = 1$, $K_m = 2$, $K_m = 4$, $K_m = 8$, and $K_m = 16$. Thus, the number of elements is increased by 2 in the following mesh considered in the convergence analysis.

To validate the numerical results, the radial stress at three different points of the interface hub–shaft: the insertion hub edge A, the opposite hub edge B, and a point placed at the half hub length (point C in Figure 2) are compared with the theoretical value of radial stress given via equation 1. Thus, the results obtained via numerical simulation are validated for a suitable value of the FE error. The variation in the contact pressure and relative error with the mesh factor is shown in Figure 3a for point C. In a similar way, the mesh convergence was also checked by considering the variation in the contact pressure with the mesh factor for both hub edges, with point A placed at the hub insertion edge and point B located at the opposite hub edge (Figure 3b).

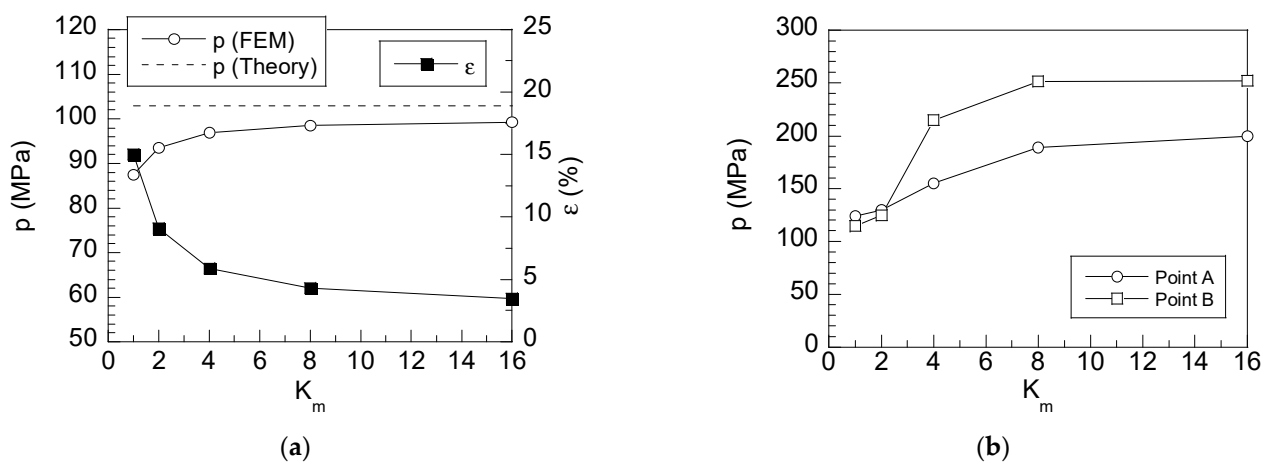


Figure 3. FE convergence testing and estimated error for dynamic FE simulations: (a) point C placed at the middle of the interface shaft–hub and (b) points A and B placed at the hub edges.

According to the results of the convergence analysis, a mesh of 4900 elements (5187 nodes) was selected for the static case simulations (Figure 1a,b). The relative error, ε , obtained for this mesh is as low as 5%. Regarding the dynamic case (Figure 1c,d), a mesh of 4736 elements (4958 nodes) is suitable for the simulations. For this mesh, the relative error, ε , is as low as 5% (Figure 3a). For the points placed at the hub edges, point A and point B, such a mesh also shows an adequate convergence in the results as Figure 3b shows. The element dimension at the contact zone is 0.8×0.8 mm for the selected mesh (Figure 2).

3. Results

For obtaining a better understanding of the influence of manufacturing conditions of a press fit on the final contact pressure at the interface shaft–hub, a comparison of four different approaches is carried out: (i) the uniform stress distribution given via theory, (ii) the stress distribution obtained in a static case with the components assembled; hence, without considering the manufacturing effects, (iii) the dynamic case where the shaft is forced to pass through the hub up to reach the final assembly position considering the linear elastic behavior of the material, and (iv) a dynamic case considering the elastoplastic material behavior, revealing the manufacturing-induced plastic strains after the assembly of a press fit. All the cases were simulated by considering them frictionless since the influence of friction will be discussed later in Section 3.2.

3.1. Stress State Distributions at the Interface Hub–shaft

The hub radial stress obtained at the interface shaft–hub is presented in Figure 4a for the diverse approaches considered. For the sake of clarity, a detailed view of the radial stress distributions at the insertion side (left edge of the hub, point A in Figure 1) is shown in Figure 4b and, in a similar way, a detailed view of the stress distributions at the surroundings of the hub edge B (right edge of the hub, Figure 1) is included in Figure 4c.

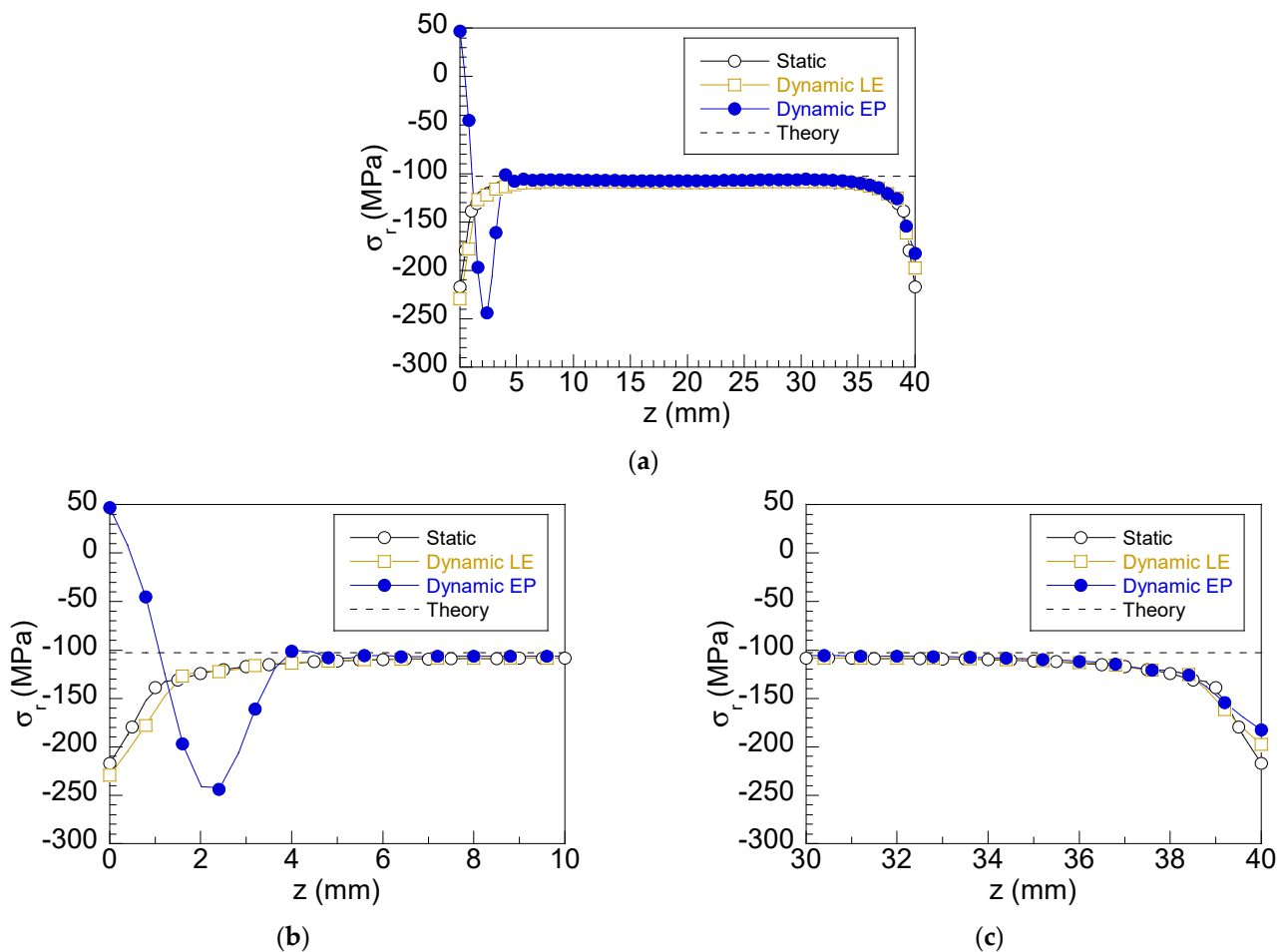


Figure 4. FEM radial stress distribution in a press fit after assembly: (a) general view; (b) detailed view of the left side (insertion), and (c) detailed view of the right side (opposite to insertion) for different numerical simulation approaches.

According to the obtained results, a high stress concentration is localized at both hub edges. However, this concentration is shown in a different way depending on the considered approach. Thus, the static case exhibits a symmetric distribution with the same stress concentration at both sides of the hub. This stress concentration is very localized at the hub edges surroundings, and, outside of them, the stress is uniformly distributed, reaching values close to the ones given via theory. In a similar way, the dynamic case considering the linear elastic approach, i.e., the insertion of the shaft into the hub is simulated without considering the plasticity effects, leads to a similar symmetrical stress distribution to the static case with soft variations: (i) lower stress concentration at both hub edges and (ii) a slightly deeper zone of stress concentration.

However, when plasticity is considered in the dynamic simulation (elastoplastic material behavior), significant changes are produced on the stress distributions. Firstly, the stress field at the interface is not symmetrical. At the insertion side (point A), the maximum radial stress is moved towards the inner points of the interface, reaching a slightly higher stress concentration than the one obtained with the linear elastic approach. In addition, positive values of radial stress are localized at hub edge A. This means a loss of contact caused by plastic strains at the hub edge where the shaft is inserted. However, at the other side of the hub (point B), the radial stress distribution is similar to the static case with the maximum value localized at the hub edge. It is worth highlighting that the stress concentration at the insertion side is lower in the static case than the one obtained for the dynamic elastoplastic case. In addition, the stress concentration is lower at the opposite side, so localized plasticity induced by manufacturing causes a stress redistribution, increasing the

stress at the insertion side and lowering the stress concentration at the hub edge localized at the opposite side. Finally, the stress at the interface out of the stress concentration zones (point C) is the same for all the approaches considered, reaching similar values to the ones given via the theory equations.

Taking these results into account, the analysis must be focused on the dynamic elastoplastic approach to find more realistic distributions by considering the effect of manufacturing-induced plastic strains. This way, the variations in the stress and strain distributions caused by friction in conventional and chamfer hubs can be clearly visualized in FE color map fields. Thus, the distributions of radial stress and equivalent plastic strains are shown in Figures 5 and 6, respectively, for the FE simulation of the press-fit assembly process considering (i) conventional hubs without friction (Figures 5a and 6a), and (ii) with friction, $\mu = 0.3$ (Figures 5b and 6b), and in a similar way, (iii) considering a chamfer hub with an optimal chamfer angle $\alpha = 15^\circ$ for the frictionless case (Figures 5c and 6c), and finally, (iv) an optimal chamfer hub with friction, $\mu = 0.3$ (Figures 5d and 6d).

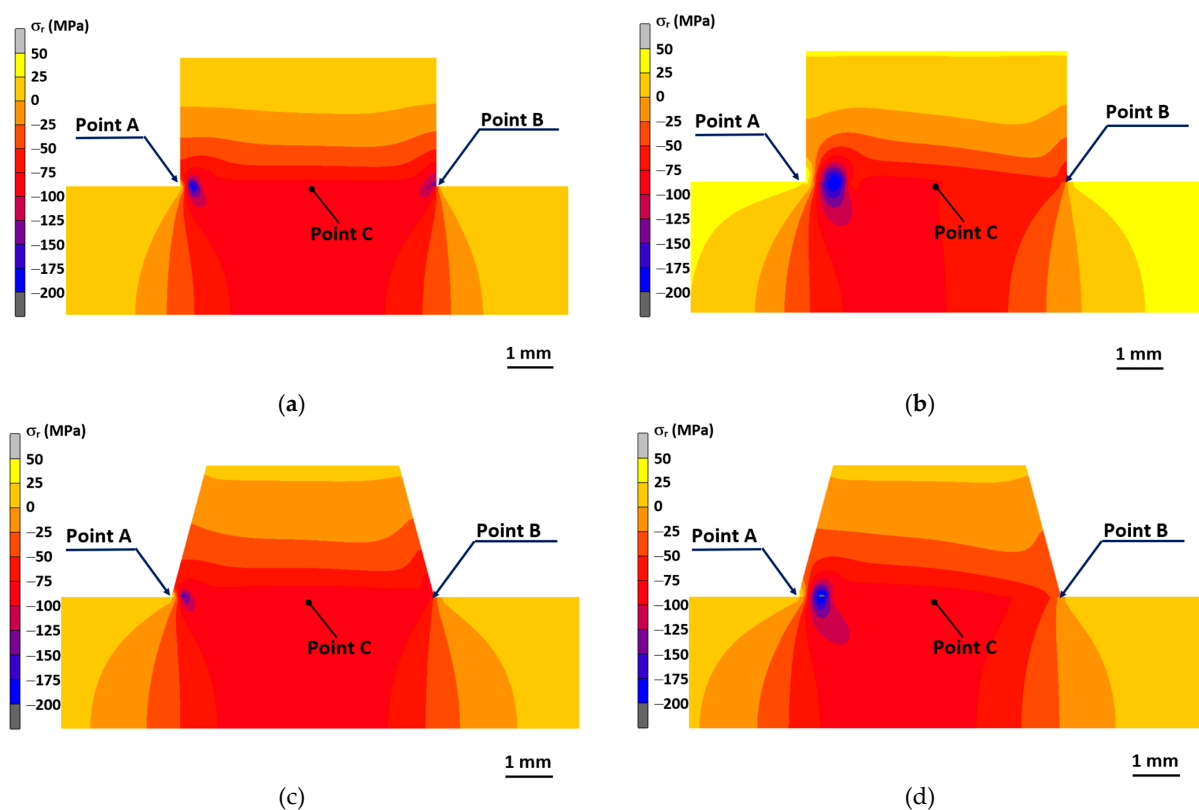


Figure 5. FEM radial stress distribution in a press fit after assembly: (a) frictionless with a conventional hub; (b) considering friction ($\mu = 0.3$) with a conventional hub; (c) frictionless with a chamfer hub, and (d) considering friction ($\mu = 0.3$) with a chamfer hub.

According to the obtained results, the previously discussed manufacturing effect on the stress distributions of conventional hubs without friction is easily observed in the stress field shown in Figure 5a. Thus, the high stress concentration zone (blue zones) is located at both hub edges and a uniform distribution of radial stress (orange zone) is observed at the middle zone of the interface. The stress concentration is more intense and more extended at the insertion side, resulting in an asymmetrical distribution as was previously observed in Figure 4a. At hub edge A, a small zone of positive radial stress is observed at the insertion side (yellow zone), revealing the zone without contact between the hub and shaft at the interface caused by plastic strains. In addition, the effects of friction and optimized chamfer hub geometry on the radial stress fields are qualitatively revealed.

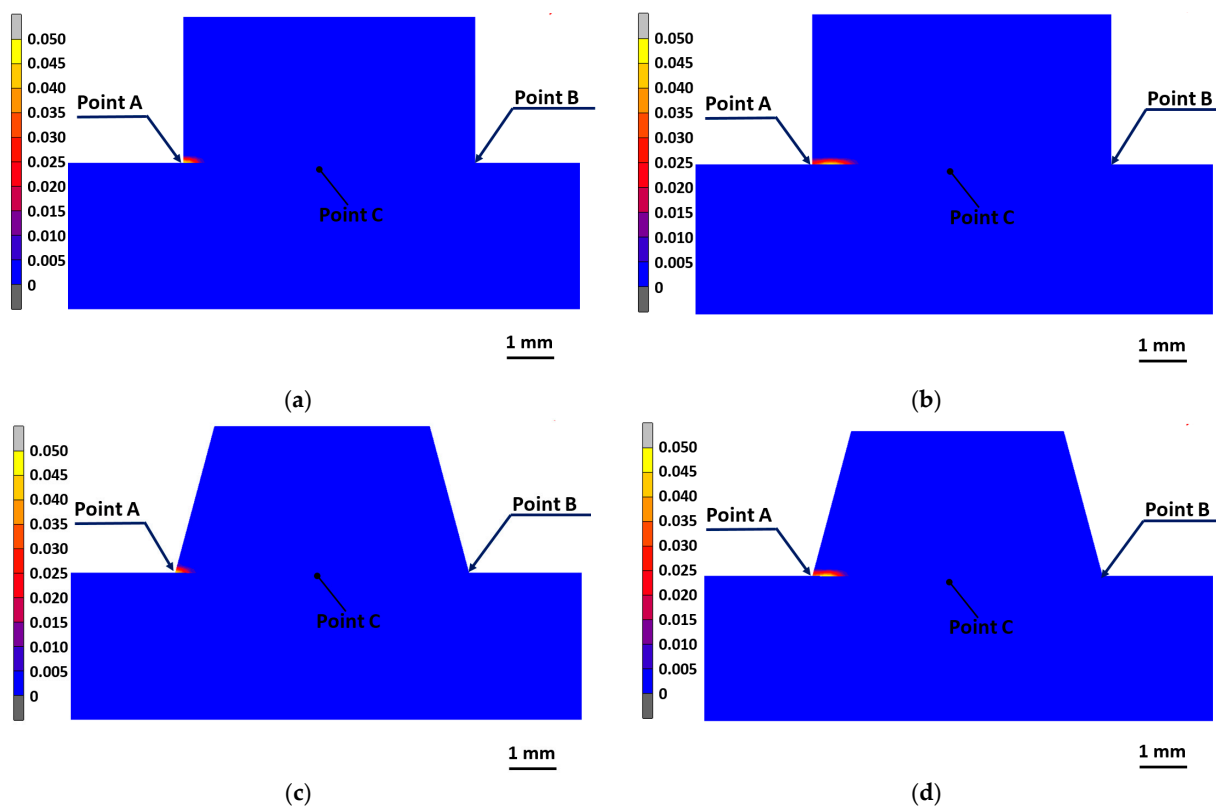


Figure 6. FEM equivalent plastic strain distribution in a press fit after assembly: (a) frictionless with a conventional hub; (b) considering friction ($\mu = 0.3$) with a conventional hub; (c) frictionless with a chamfer hub, and (d) considering friction ($\mu = 0.3$) with a chamfer hub.

This way, friction causes significant effects on the radial stress field: (i) the stress concentration at the insertion side is more intense and more extended than the one corresponding to the frictionless case (Figure 5a), (ii) the no contact hub–shaft zone at the insertion hub edge is increased (yellow zone), (iii) the stress concentration at the opposite side is significantly reduced (no blue zone is observed in Figure 5b at point B), and (iv) a non-uniform distribution of radial stress appears at the middle zone of the interface. This way, a redistribution of stress at the interface shaft–hub appears as a consequence of the increment of the radial stress at the insertion side. Therefore, friction is a high influencing parameter on stress distributions in a press fit.

Figure 5c shows the beneficial effects of optimal chamfer geometry on radial stress fields for the frictionless case. This way, the stress concentration at the insertion side is reduced (blue zone in Figure 5c) and the stress concentration at the opposite side disappears (no blue zone). Out of the stress concentration zones, a uniform stress distribution is localized at the central zone of the interface in a similar way to conventional hubs (Figure 5a). Regarding the chamfer hub case considering friction, the stress concentration at the insertion side is higher than the one obtained in the frictionless case (Figure 5c), but such a stress concentration is lower than the one obtained in the conventional hub (Figure 5a). In addition, the stress concentration on the opposite side is also reduced due to the combined effect of chamfer hub geometry and friction. Finally, the radial stress at the middle zone of the interface is non-uniformly distributed due to stress redistribution.

As previously discussed, plastic strains play a relevant role in the radial stress distributions at the interface shaft–hub. So, the analysis of the plastic strain fields shown in Figure 6 reveals that a plastic zone at the insertion side is generated in the hub during the manufacturing of a press fit in both conventional hubs (Figure 6a) and chamfer hubs (Figure 6c). The plastic zone is mainly extended in the axial direction (around 10–15% of

the interface length) where both surfaces, hub and shaft, are in contact; additionally, it is narrow in the radial direction.

In chamfer hubs, the plastic strains are lower and less extended in the radial and axial direction than in conventional hubs. This way, the beneficial effect of the modified hub geometry is revealed. Friction causes a more intense and more extended plastic zone for both hub geometries (Figure 6b,d), but the effect is lower in chamfer hubs, resulting in lower plastic strains and a less extended plastic strain zone than the one obtained in conventional hubs. To go further in the analysis, the histograms of the radial stress and plastic strain during the manufacturing process of a press fit are shown in Figure 7 at the main points of the interface hub–shaft; namely, the hub edge at the insertion side (point A, Figure 7a,b), the hub edge opposite to the insertion side (point B, Figure 7c,d), and finally, point C placed at the middle of the interface hub–shaft (Figure 7e,f).

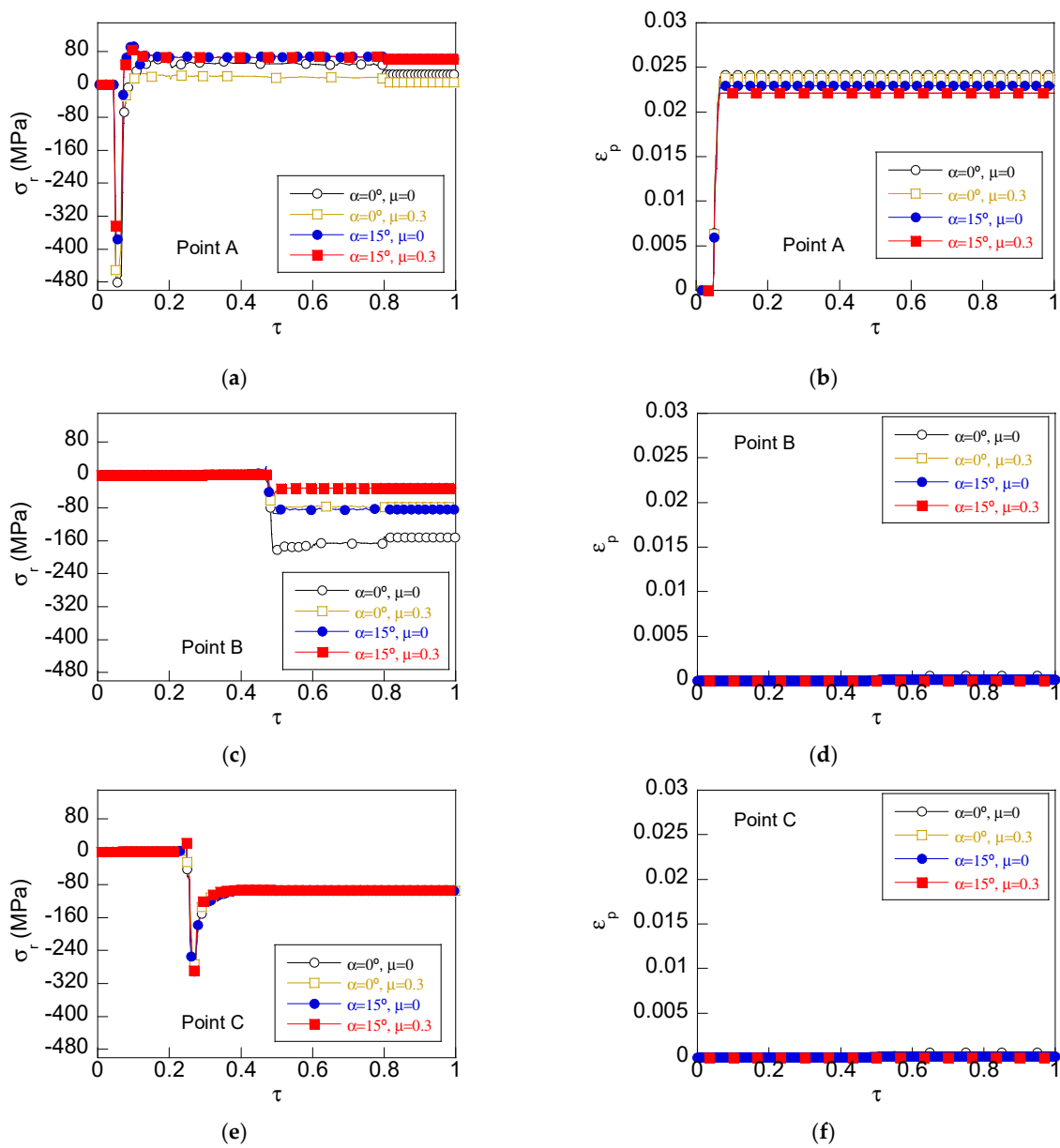


Figure 7. Histograms of (a) radial stress and (b) equivalent plastic strain for the hub edge placed at the insertion side; (c) radial stress and (d) equivalent plastic strain at a point placed at the middle of the interface, and (e) radial stress and (f) equivalent plastic strain at a point placed at hub edge point B.

According to the obtained results, the radial stress at point A is suddenly increased when the shaft is inserted into the hub, reaching values higher than the material yield strength, and hence, causing plastic strains. Such plastic strains reduce the initial radial dimensions of the hub and, this way, a radial interference is generated. At this instant, the contact zone hub–shaft, i.e., the contact zone between the shaft and hub (interface), is so small, and consequently, a high stress is produced, causing plasticity.

Conventional hubs have the same hub thickness at the hub edges and at inner points; however, chamfer hubs have an increasing thickness with an axial coordinate at the chamfer zones. This way, during the insertion of the shaft at hub edge A, the opposition of the chamfer hub geometries (low thickness at the surroundings of point A) to be adapted to the new dimensions is lower than the opposition of a conventional hub with a higher thickness at the insertion side. As a result, the radial stress (equivalent to contact pressure) is lower in chamfer hubs (Figure 7a) than the one in conventional hubs. Consequently, the plastic strains generated in chamfer hubs are lower (Figure 7b) since the transition to the new dimensions is softer and more progressive due to chamfer geometry. Afterwards, as the contact zone is increased, the radial stress is progressively reduced up until it reaches a positive value of radial stress, causing a loss of contact between the hub and shaft at this zone due to localized plasticity.

At the opposite side of the insertion zone (point B, Figure 7c,d), a similar trend is observed when the shaft is contacting hub edge B. This way, an increase in the radial stress is produced, being higher for the cases of higher opposition to the adaptation to the new radial dimensions (conventional hubs) than in chamfer hubs. At this side, the effect of friction is more significant since friction causes a stress redistribution at the interface shaft–hub, lowering the radial stress at hub edge B as a result of the increase in stress at the insertion side. Finally, the variations in the radial stress at the point placed in the middle of the shaft–hub interface are not significant for all the cases of study since at this point no plastic strains are generated (Figure 7e,f).

3.2. Influence of the Friction Coefficient on the Stress Distributions

According to the previously discussed results, friction plays a key role in producing significant changes in the stress and strain distributions at the interface shaft–hub. To go deep into the analysis, the influence of friction on the stress and strains distributions at the interface is analyzed in terms of the friction coefficient by considering both conventional and chamfer hubs. To achieve this goal, the friction coefficient was varied from the frictionless case to a high friction case according to the following sequence: (i) $\mu = 0$, frictionless; (ii) hydrodynamic lubrication, $\mu = 0.01$; (iii) boundary lubrication, $\mu = 0.1$; (iv) $\mu = 0.2$; (v) $\mu = 0.3$, common value for friction with steel–steel contact; (vi) $\mu = 0.4$; and finally, (vii) $\mu = 0.5$, a case with the highest friction. The resulting radial stress distributions in terms of the dimensionless axial coordinate ζ (defined as $\zeta = z/l$) at the interface are shown in Figure 8 for conventional hubs (Figure 8a) and for chamfer hubs with an optimal chamfer angle (Figure 8b). In a similar way, Figure 9 shows the equivalent plastic strain distributions for both hub geometries.

According to the results shown in Figure 8, the influence of the friction coefficient is revealed. For a better understanding, three different zones are considered in terms of the dimensionless axial coordinate ζ : firstly, the zone nearby the insertion side ($0 < \zeta < 0.2$); secondly, the stress concentration zone at the opposite side ($0.8 < \zeta < 1$); and finally, the middle zone between stress concentration zones at the hub edges ($0.2 < \zeta < 0.8$).

A similar asymmetrical distribution to the previously discussed one in Figure 4 is obtained with different stress concentrations at both hub edges. However, significant changes are observed in the radial stress as the friction coefficient is varied. Thus, on one hand, for friction coefficients lower than $\mu < 0.2$, the maximum radial stress at the insertion side is progressively increased with the friction coefficient, and for higher values of the friction coefficient, the variations are softer. In addition, the place where the maximum stress is located is progressively deeper with soft variations for $\mu < 0.2$, and for higher

friction coefficients, it is highly increased. This effect is linked to the extension of the plastic zone as will be discussed later. So, at the insertion side, friction causes both an increment of stress concentration and a wider zone of high stresses.

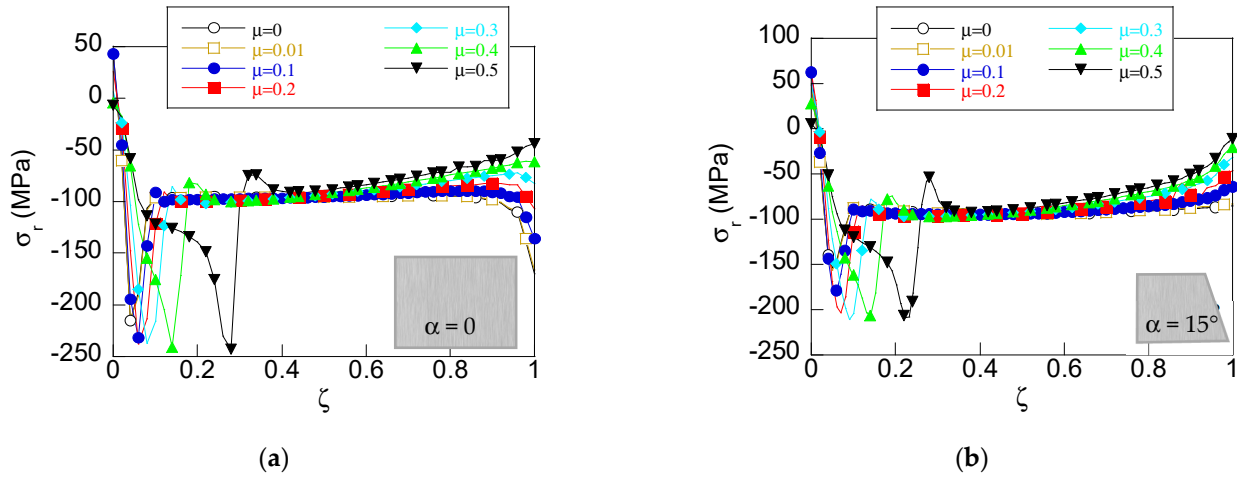


Figure 8. FEM radial stress distribution in a press fit after assembly for diverse friction conditions in (a) a conventional hub; (b) a chamfer hub ($\alpha = 15^\circ$).

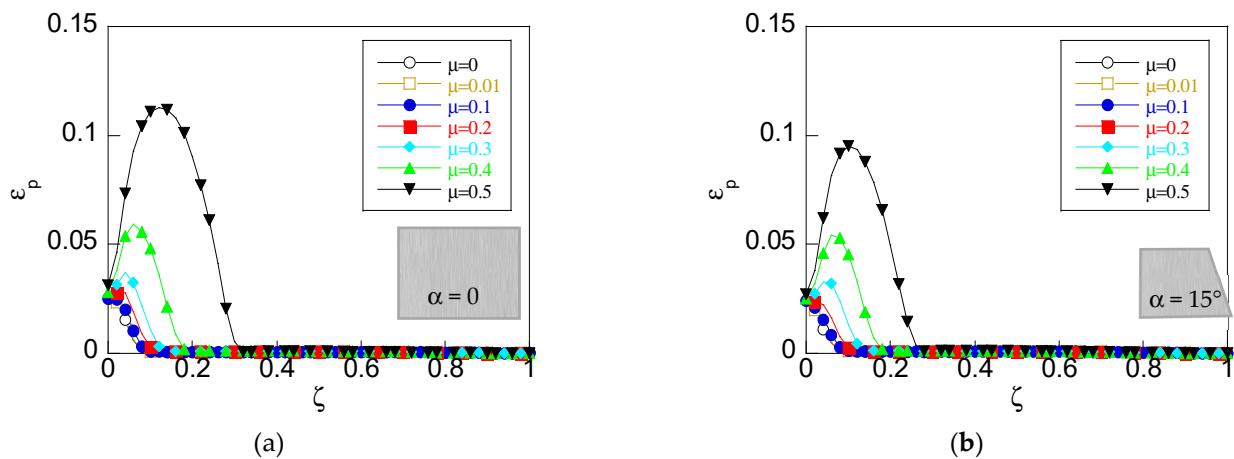


Figure 9. FEM equivalent plastic strain distribution in a press fit after assembly for diverse friction conditions in (a) a conventional hub; (b) a chamfer hub ($\alpha = 15^\circ$).

On the other hand, significant changes are produced in the stress concentration at hub edge B. This way, the stress concentration is progressively reduced as the friction coefficient is increased. As a result, the stress concentration disappears for friction coefficients higher than $\mu > 0.3$, obtaining radial stress values lower than the ones given via the theory; hence, the stress concentration at this side is annulled. Finally, at the middle zone of the interface, the uniform stress distribution obtained for the frictionless case is progressively modified as friction is increased due to the reduction in radial stress at the opposite side of the hub. Thus, the radial stress at the middle zone of the interference is linearly decreased as the distance from the insertion hub edge is increased. This way, the contact pressure is progressively reduced as the local axial coordinate ζ increases up to reach the lower values of stress observed at hub edge B. This effect is more significant for high values of the friction coefficient.

According to these results, friction increases the stress concentrations at the insertion zone and, as a consequence, a stress redistribution is produced at the interface with significant reductions at the opposite side and a progressive transition in the middle zone of the interface shaft–hub between both stress concentrations. As a result, the asymmetry

of the radial distribution is increased with the friction coefficient. This is a non-desirable scenario since this asymmetrical distribution produces a non-uniform contact pressure that can cause vibrations and a non-adequate performance of the assembly leading to fatigue and fracture.

Similar effects are observed for the chamfer hub cases, but in a less accused way. Thus, the stress concentration at the insertion zone is lower (about 20%) than the one obtained in conventional hubs due to the beneficial effect of the chamfer geometry. Friction increases the stress concentration for $\mu < 0.2$ in a similar way as observed for conventional hubs with soft variations for higher friction coefficients. The depth of the maximum stress is slightly lower for chamfer hubs. However, the main changes appear at the opposite side, showing the beneficial effect of chamfer hub geometry. As can be seen in the stress distribution corresponding to the frictionless case, the radial stress values at hub edge B are similar to the radial stress obtained at the middle of the interface (point C); hence, the stress concentration is annulled without lowering the contact pressure. As the friction coefficient is increased, the radial stress at this hub edge is progressively reduced as it was previously observed in conventional hubs but, in this case, the reduction is more accused due to the effect of chamfer geometry. This way, for chamfer hubs with friction, the high reduction in the stress concentration (as high as 85% for the highest friction considered) is due to the combined action of both the chamfer hub geometry and friction reducing the stress concentrations. Therefore, the stress distribution at the middle of the interface between both hub edges is progressively decreased with the friction coefficient in a similar way as previously discussed for conventional hubs.

The increment of the stress concentration and the displacement of the maximum stress towards inner points can be linked to the plastic strains caused during the manufacturing of a press fit. Thus, in the plots shown in Figure 9, a plastic zone is generated at the surroundings of the hub insertion edge with null plastic strains at both the inner points of the interface shaft–hub and at the opposite side of the insertion edge.

According to the results, the maximum plastic strain is placed at hub edge A for low friction coefficients. However, for $\mu > 0.2$, the maximum plastic strain appears at inner points, increasing notably to the size of the plastic zone. The size of the plastic zone is progressively increased with friction, reaching about 30% of the extension of the interface for the highest friction cases. These sizes are linked to the displacement of the maximum radial stress observed for high friction cases. The effects of friction on plastic strains in chamfer hubs are similar to the ones discussed for conventional hubs, but reaches lower values of plastic strains (about a 10% lower) and reduces the size of the plastic zone with regard to conventional hubs. Thus, the chamfer hub geometry enhances the progressive adaptation to the dimensions of the shaft during the insertion process, causing lower plastic strains and a less extended plastic zone.

3.3. Influence of the Hub Thickness on the Stress Distributions

To reveal the influence of hub thickness on the radial stress distributions after the assembly of a press fit with conventional and chamfer hubs, diverse geometries were considered in terms of the dimensionless hub thickness γ as follows: (i) low hub thickness, $\gamma = 0.25$; and four intermediate thicknesses, (ii) $\gamma = 0.375$, (iii) $\gamma = 0.50$; the conventional case, (iv) $\gamma = 0.75$; and finally, a high hub thickness (v) $\gamma = 1$, with a thickness equal to the shaft diameter. The resulting radial stress distributions at the interface are shown in Figure 10 for conventional hubs and chamfer hubs by considering the frictionless case (Figure 10a,b) and the friction case with $\mu = 0.3$ (Figure 10c,d). In a similar way, Figure 11 shows the distributions of equivalent plastic strain at the interface shaft–hub.

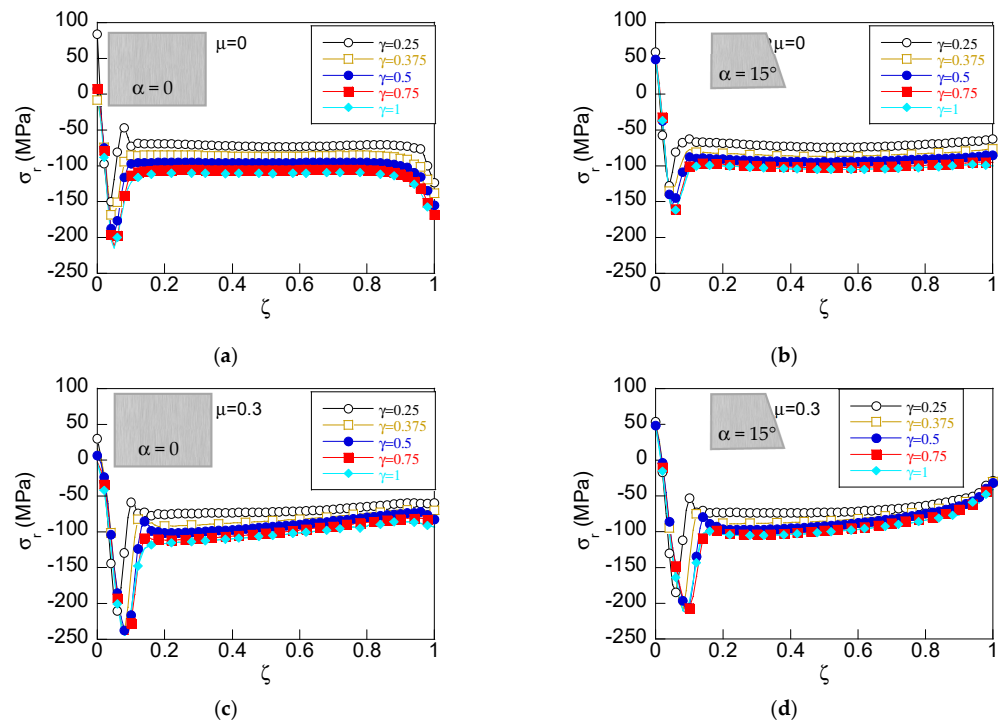


Figure 10. FEM radial stress distribution in a press fit after assembly: (a) frictionless with a conventional hub; (b) frictionless with a chamfer hub; (c) considering friction ($\mu = 0.3$) with a conventional hub, and (d) considering friction ($\mu = 0.3$) with a chamfer hub.

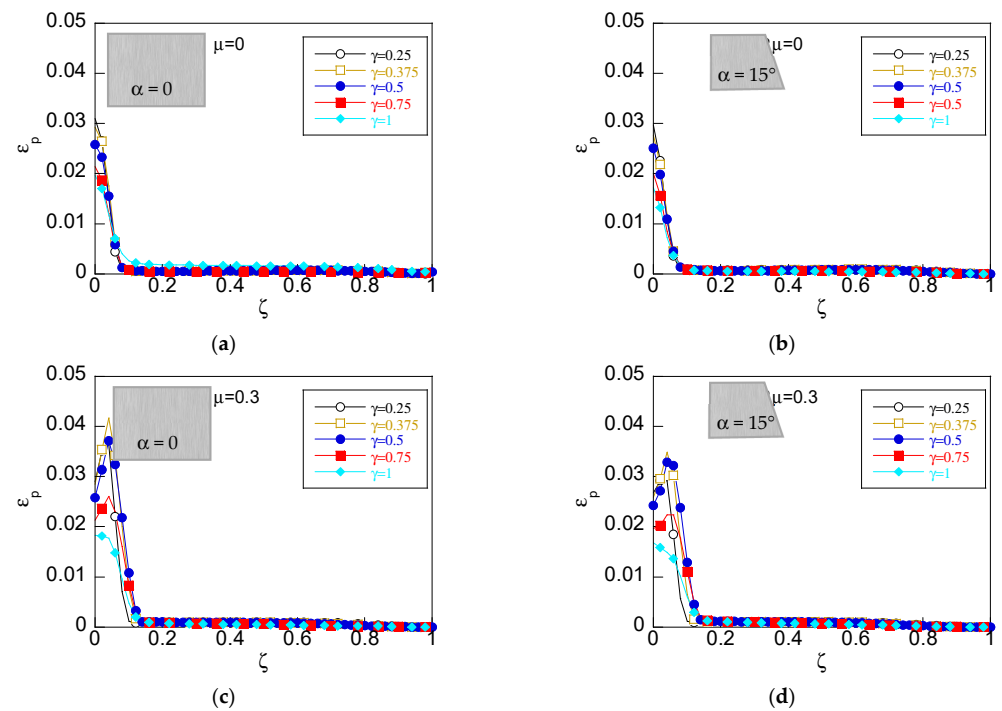


Figure 11. FEM equivalent plastic strain distribution in a press fit after assembly: (a) frictionless with a conventional hub; (b) frictionless with a chamfer hub; (c) considering friction ($\mu = 0.3$) with a conventional hub, and (d) considering friction ($\mu = 0.3$) with a chamfer hub.

Three zones can be observed in the stress distributions (Figure 10) as previously discussed. In both conventional and chamfer hubs considering frictionless contact (Figure 10a), the maximum radial stress at the insertion hub edge is progressively increased with the hub thickness, γ , as can be expected according to equation (1). However, the radial stress

values obtained considering chamfer hubs are lower (about 25%) than the ones obtained in conventional hubs, revealing the beneficial effect of the chamfer hub geometry. In addition, for hub thickness $\gamma < 0.5$ in both conventional and chamfer hubs, a displacement of the maximum radial stress is observed, and for high hub thickness, $\gamma > 0.5$, the maximum radial stress is placed at the same depth.

At the opposite side of the insertion hub edge, different stress distributions are obtained due to the effect of the geometry of the chamfer hub. Thus, the values of radial stress are progressively increased with γ in conventional hubs, revealing a similar stress concentration for all the hub thicknesses considered. In the case of chamfer hubs, a remarkable decrement of the stress concentration is observed, obtaining stress values similar to the ones given via theory; hence, the stress concentration is annulled for all the hub thicknesses analyzed. Finally, a uniform distribution of radial stress is obtained at the central zone of the interface shaft-hub in conventional hubs. In the case of chamfer hubs, a similar uniform distribution is obtained with soft variations at the edges in a similar way for all the hub thicknesses considered. For both geometries, the radial stress is increased with the hub thickness γ , reaching values closer to theoretical values.

The previously discussed effects of friction are observed in conventional hubs (Figure 10c) and chamfer hubs (Figure 10d) by considering different hub thicknesses. Thus, the maximum radial stress is gradually increased with γ (about a 25%) at the insertion side for low hub thickness and only minor variations are obtained for high hub thickness. However, the main variations with the hub thickness are observed at the place where the maximum stress is located. Thus, this maximum is progressively moved towards the inner points for $\gamma < 0.5$ and only slight variations are observed for $\gamma > 0.5$.

On the opposite side of the hub insertion edge, friction causes a noticeable decrease in the stress concentration. This reduction is similar for all the hub thicknesses, annulling the stress concentration at hub edge B. In the case of chamfer hubs, a combined effect of chamfer and friction reduces the stress concentration in a significant way. As a result, a similar reduction in stress for all the hub thicknesses is obtained, reaching even lower values than the stress at the central points (no stress concentrations).

Finally, at the central zone of the interface shaft-hub, the same effect of hub thickness on radial stress previously discussed for the frictionless case is observed with a progressive decrement of the contact pressure as the hub thickness is increased. The main effect of friction at this zone is a slight decrement of radial stress with the axial coordinate ζ in the same manner observed in the previous section, resulting in a non-uniform distribution. This stress decrement with ζ is not dependent on the hub thickness. This way, the effect of chamfer geometries is again revealed, reducing the stress state at the shaft-hub interface and lowering the increments of stress caused by friction.

The plastic strain distributions shown in Figure 11 reveal the effects of hub thickness on frictionless cases: (i) a reduction in the maximum plastic strain as the hub thickness is increased and (ii) a slight increment of the plastic zone with the hub thickness. Notice that for all the frictionless cases (Figure 11a,b), the maximum plastic strain is placed at hub edge A.

In chamfer geometries, the plastic strains are lower (about a 5%) than the ones corresponding to conventional cases and the size of the plastic zone is similar for all the hub thicknesses considered. However, for the friction cases, a different trend is observed, as for a hub thickness $\gamma < 0.5$, the maximum plastic strain is increased, and for a high hub thickness $\gamma > 0.5$, the plastic strain is reduced, resulting in a more uniform distribution.

In addition, friction causes in both hub geometries (Figure 11c,d) a displacement of the maximum plastic strain towards the inner points of the interface, enlarging the plastic zone for high hub thicknesses. However, in chamfer hub cases, the plastic strains are lower (about 15%) than conventional hubs and the plastic zone is similar for all the hub thicknesses considered. Therefore, friction causes an increment of the plastic strains and a less uniform distribution of plastic strains with the maximum plastic strain placed out of hub edge A, and consequently, an increment of the extension of the plastic zone. Chamfer

geometries reduce the magnitude of plastic strains with slight reductions in the extension of the plastic strain zone.

3.4. Influence of the Radial Interference on the Stress Distributions

Finally, the influence of the interference closure on stress distributions after the assembly of a press fit was analyzed in terms of radial interference, δ . Thus, several interference fits recommended by the ISO standard [33] for the given shaft diameter of 40 mm were selected as follows: (i) 40H7r6, $\delta = 25 \mu\text{m}$; (ii) 40H7s6, $\delta = 29.5 \mu\text{m}$ (reference case); (iii) 40H7t6, $\delta = 32 \mu\text{m}$; (iv) 40H7u6, $\delta = 38 \mu\text{m}$; and finally, (v) 40H7x6, $\delta = 48 \mu\text{m}$. The resulting radial stress distributions at the interface are shown in Figure 12 for conventional hubs and chamfer hubs by considering the frictionless case (Figure 12a,b) and the friction case with $\mu = 0.3$ (Figure 12c,d). In a similar way, Figure 13 shows the equivalent plastic strain distributions.

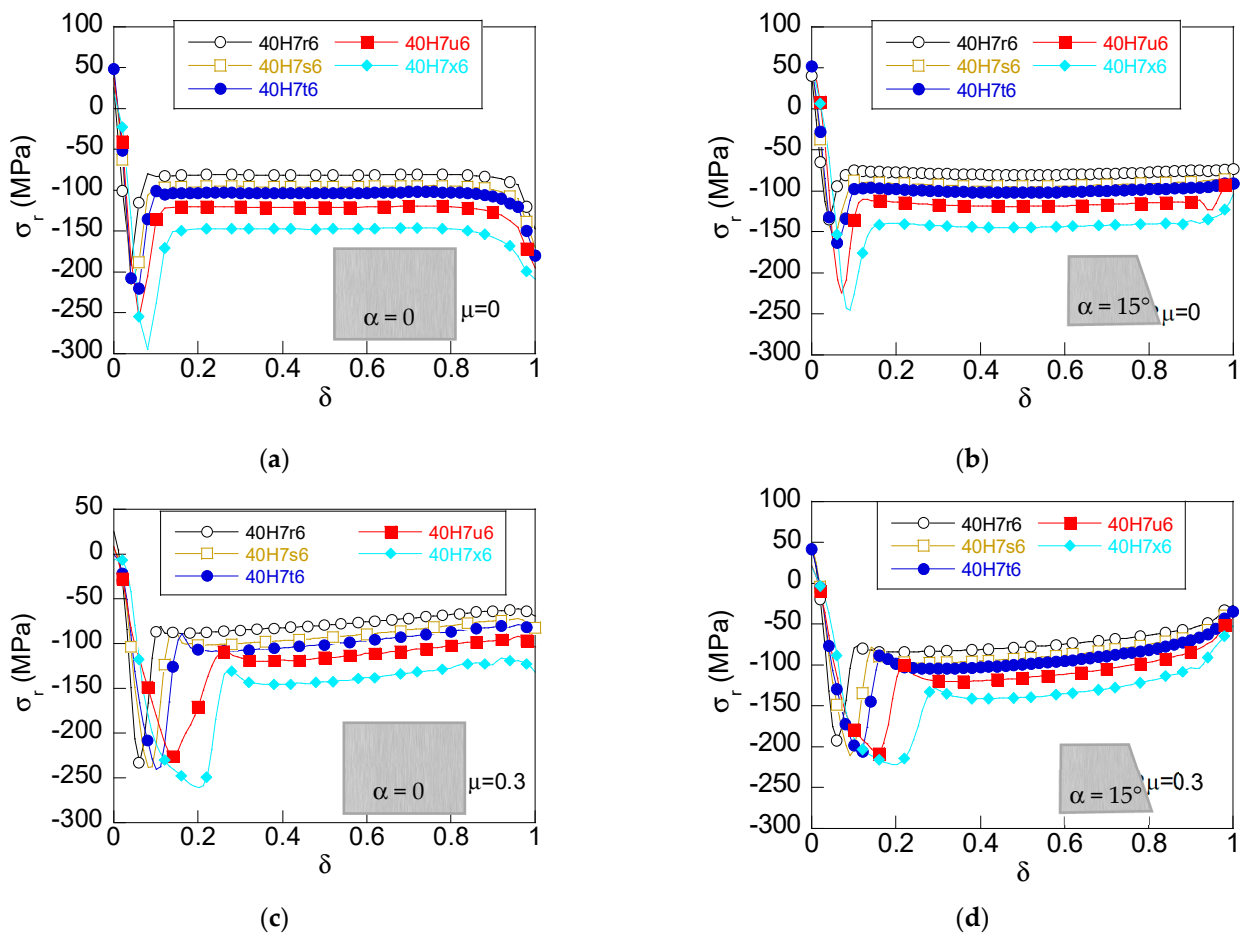


Figure 12. FEM radial stress distribution in a press fit after assembly for diverse radial interferences: (a) frictionless with a conventional hub; (b) frictionless with a chamfer hub; (c) considering friction ($\mu = 0.3$) with a conventional hub, and (d) considering friction ($\mu = 0.3$) with a chamfer hub.

The distributions of radial stress obtained for diverse radial interferences in the frictionless cases show the three zones clearly differentiated at the insertion hub edge, the opposite hub edge, and the central zone of the interface. This way, the higher the radial interference, δ , the higher stress concentration at hub edge A. In addition, the zone of high stress is also increased with radial interference.

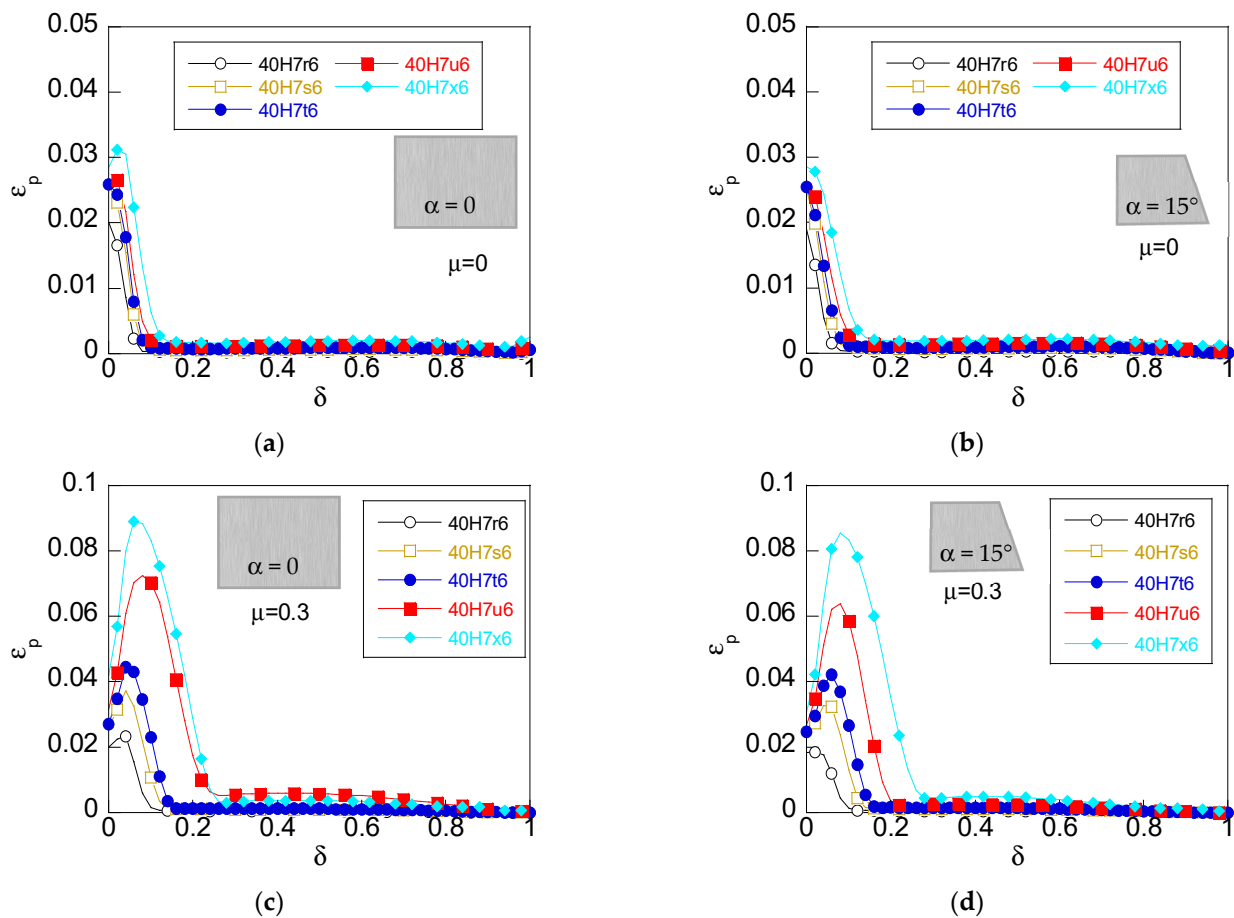


Figure 13. FEM equivalent plastic strain distribution in a press fit after assembly for diverse radial interferences: (a) frictionless with a conventional hub; (b) frictionless with a chamfer hub; (c) considering friction ($\mu = 0.3$) with a conventional hub, and (d) considering friction ($\mu = 0.3$) with a chamfer hub.

In the case of the chamfer hub, lower values of stress than the ones corresponding to conventional hubs are obtained due to the stress-relieving effect of the optimal chamfer hub. The radial stress is uniformly distributed at the middle point of the interface, reaching values similar to the ones given via theory (equation 1) for both hub geometries. Notice that radial interference is directly dependent on contact pressure; hence, for higher δ , a higher contact pressure is expected. On the opposite side of the hub, a stress concentration is also observed without significant changes with radial interference for conventional hubs. However, notable changes are produced in chamfer hubs, annulling the stress concentration. This stress reduction is slightly higher for high radial interferences; as a result, the stress values at the hub edge are lower than the stress at the middle point of the interface shaft–hub. This can be linked to the increment of stress concentration previously commented at the insertion zone, leading to a redistribution of stresses at the central zone of the interface.

The effect of friction is mainly observed as a displacement of the maximum radial stress towards the inner points of the shaft–hub interface since the values of maximum stress are almost the same for all the radial interferences considered for both hub geometries. At the middle of the interface shaft–hub, friction causes a slight decrement of the radial stress with the axial coordinate ζ for all the radial interferences considered. The slope at this zone is similar for all the cases considered with diverse δ . This effect is also observed in chamfer hubs. In addition, friction causes significant changes in the radial stress at hub edge B, with notable reductions (50%) that annulled the stress concentration. Thus, values similar to the ones obtained at central points of the interface are reached even for low radial

interferences, δ . In chamfer hubs, this stress reduction is even higher (60%) as a result of the synergistic effect of friction and chamfer geometry, obtaining stress values lower than the ones located at the central zone. This effect can be linked to the transition between both hub edges: the insertion edge A, with a high stress concentration, and the opposite hub edge B, with a significant relief of stress concentration.

Finally, for frictionless cases, the plastic strain exhibits a maximum located at hub edge A for all the radial interferences analyzed (Figure 13a,b). The plastic strain is progressively decreased with the axial coordinate until it becomes null, delimiting the size of the plastic zone. Thus, the increase in radial interference causes both an increment of plastic strains and an increment of the size of the plastic zone for both hub geometries for the frictionless case. However, slightly lower plastic strains are observed (about 5%) in the case of chamfer hubs. An exception to this rule is the frictionless case with the highest δ considered, where the maximum plastic strain is located at inner points.

However, friction significantly changes the plastic strain distributions for the diverse radial interference considered in both conventional and chamfer hubs. Thus, the maximum plastic strain is located at inner points even for the lowest radial interferences considered. In addition, as the radial interference δ is increased, the place of the maximum plastic strain is progressively moved towards the inner points of the interface. This way, the plastic zone is wider for high radial interference, δ , cases. In the case of chamfer hubs, the values of plastic strains are lower (about a 10%) than the ones obtained in conventional hubs. Furthermore, the maximum plastic strain is also increased with the radial interference. These changes can be linked to the variations shown in previously discussed radial stress concentration plots since the maximum plastic strains are located at the same position of the maximum radial stress (Figure 12).

4. Discussion

In order to find out the role of the friction coefficient in the contact pressure, the variations in such a variable with the friction coefficient are plotted in Figure 14 for diverse chamfer hubs with chamfer angles varied from $\alpha = 0^\circ$ (conventional hub) up to $\alpha = 20^\circ$. Contact pressure was obtained as the area enclosed by the radial stress distributions plotted in Figure 8.

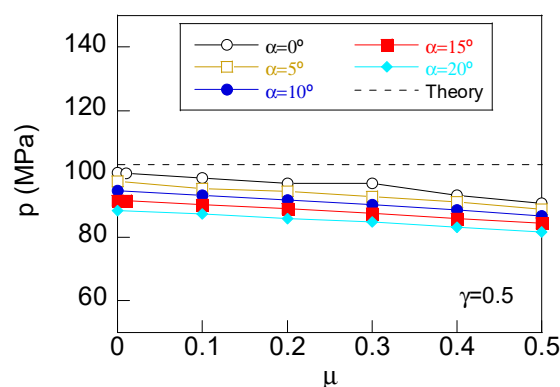


Figure 14. Variation in the contact pressure with the friction coefficient in interference fits with chamfer hubs for diverse chamfer hub angles.

According to the obtained results, the contact pressure in conventional hubs considering frictionless contact is similar to the value given via theory. As friction is increased, a slight linear decrement of contact pressure with the friction coefficient (about 10% for the highest friction coefficient considered) is observed for conventional hubs ($\alpha = 0^\circ$). A similar linearly decreasing trend is obtained as the friction coefficient is increased for chamfer hubs. In addition, the contact pressure is softly reduced (about 8%) as the chamfer angle is higher. Thus, for the optimal chamfer angle $\alpha = 15^\circ$, a decrement of 15% of contact pressure is obtained for the highest friction coefficient. These reductions are linked to the loss of

contact pressure at the opposite side to the insertion edge where the stress concentration is annulled using either chamfer hubs (see values in Figure 8 for $\mu = 0$) or by the action of friction (see values in Figure 8 for $\mu = 0.3$ for any chamfer angle, α). So, the non-symmetrical radial stress distribution induced by manufacturing does not significantly affect the contact pressure due to stress redistribution.

In a similar way, the influence of the hub thickness on contact pressure is shown in Figure 15. In this figure, the variations in contact pressure with the hub thickness are plotted for different friction coefficients in conventional hubs (Figure 15a) and optimal chamfer hubs (Figure 15b). Contact pressure was obtained as the area enclosed by the radial stress distribution in Figure 10. Additional cases were simulated in a similar way as previously discussed in Section 3.3, considering different friction coefficients according to the sequence from $\mu = 0$ (frictionless) to $\mu = 0.5$ representing the highest friction.

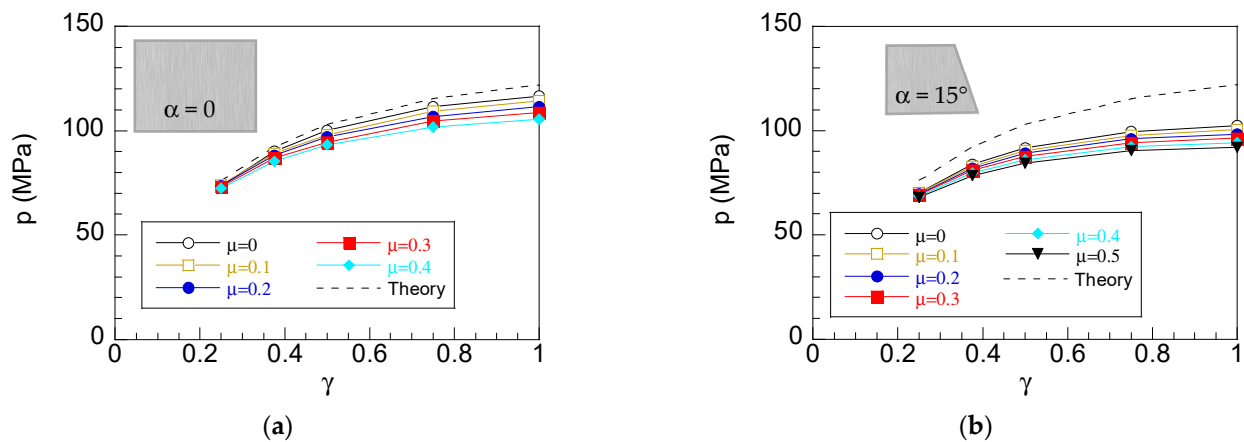


Figure 15. Variation in the contact pressure with the dimensionless hub thickness in interference fits for (a) conventional hubs and (b) a chamfer hub with an optimal chamfer angle, $\alpha = 15^\circ$.

Contact pressure is non-linearly increased with the hub thickness according to equation (1). This way, for low hub thicknesses, the variation is high, and for hub thickness higher than $\gamma = 0.5$ (the most common dimensions of hubs), this growth is smoother. This trend is observed for both conventional hubs and chamfer hubs. In general terms, the contact pressure is lower as the friction coefficient is higher. This reduction depends on the hub thickness. This way, the reduction is low, about 4%, for low hub thickness and the reduction is increased up to 15% for high thickness. The reduction is not significant (10%) for common values of a hub thickness $\gamma = 0.5$. This loss of contact pressure is linked to the effects of friction on the stress distributions previously discussed, causing a reduction in stress at the opposite hub edge B and a loss of contact pressure at the plastic zone. The loss of contact pressure is more significant in chamfer hubs, reaching 15% for low hub thickness and a reduction as high as 25% for high hub thickness. For $\gamma = 0.5$ (the commonly used value of hub thickness), the reduction is 10% for the frictionless case and about 18% for the highest friction considered. This loss of contact pressure is linked to the significant reduction in contact pressure at the hub edges due to the chamfer geometry at both edges of the hub and the combined action of friction and chamfer geometry on the stress reduction at the opposite hub edge B. So, considering these results, the use of hubs with a thickness higher than $\gamma = 0.5$ is not recommended in press fits using chamfer hubs due to the high loss of contact pressure.

Finally, the variation in the contact pressure with the radial interference is shown in Figure 16, considering different friction coefficients for conventional hubs (Figure 16a) and optimal chamfer hubs (Figure 16b). In a similar way, the contact pressure was obtained as the enclosed area of the radial stress distributions shown in Figure 12. To achieve more general results, additional cases were simulated considering different friction coefficients.

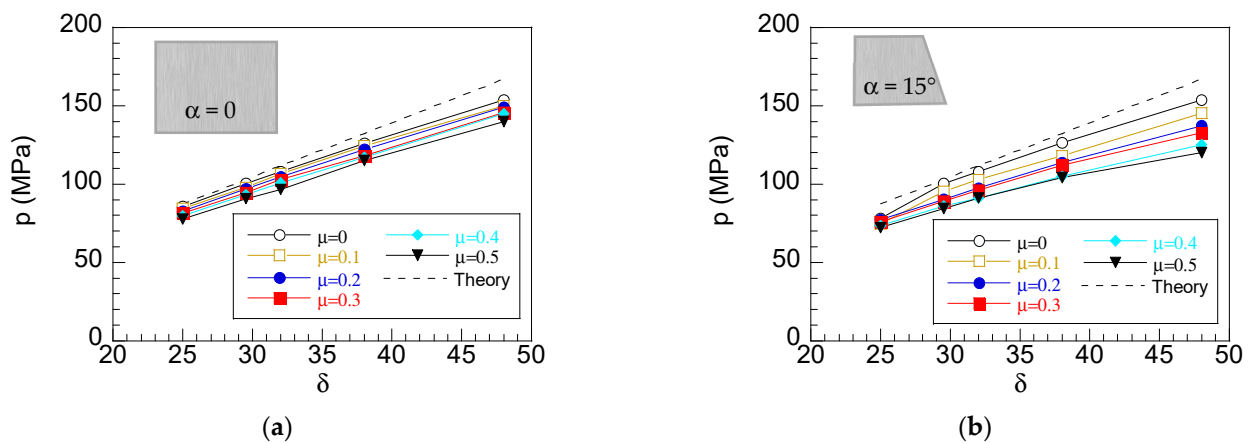


Figure 16. Variation in the contact pressure with the radial interference in press fits for (a) a conventional hub and (b) a chamfer hub with an optimal chamfer angle, $\alpha = 15^\circ$.

The results show a linear increment of contact pressure with radial interference as could be expected according to the linear dependence shown in equation 1. The effect of friction is shown as a progressive loss of contact pressure as the friction coefficient is increased. This loss is caused by the stress reductions at the opposite hub edge B shown in Figure 12. This reduction is dependent on radial interference; thus, for low values of δ , a slight loss of contact pressure is obtained even for the highest friction coefficient (10%). However, the loss of contact pressure for high values of radial interference is as high as 15% for the highest friction considered. These effects are also observed in chamfer hubs, but the differences are more significant with the loss of contact pressure as high as 28% for the highest radial interference (H7x6). This higher loss of contact pressure is due to the huge decrease in radial stress at hub edge B where the combined action of friction and chamfer geometry appears and the reduction at the insertion hub edge caused by the chamfer geometry. Anyway, the loss of contact pressure is around 15% for low radial interferences (H7r6, H7s6, or H7t6). So, in order to avoid a significant reduction in contact pressure, the use of high radial interferences with chamfer geometries in press fits is not recommended. However, for low radial interferences, the loss of contact pressure is not significant, and consequently, chamfer hubs can be used.

5. Conclusions

In this study, the numerical simulations of the mechanical assembly of a press fit revealed the key role of manufacturing-induced stress and plastic strain fields on the contact pressure at the interface shaft–hub considering conventional and optimized hub geometries. Thus, the manufacturing of a press fit in conventional hubs without friction causes a non-uniform asymmetrical distribution of radial stress at the shaft–hub interface with huge stress concentrations (110% higher than the one given via theory) placed nearby the hub edge at the insertion side. However, the stress concentration at the opposite side of the hub, hub edge B, is lower (66% higher than the one given via theory) due to the stress redistribution and the stress outside of the surroundings of the hub edges is uniformly distributed as the design equations predict. The manufacturing of a press fit causes plastic strains at the insertion hub edge; being the size of the plastic zone, it is wider in the axial direction and narrow in the radial direction.

Friction causes a significant increment of both the maximum plastic strains (50%) and the size of the plastic zone (100%). In addition, the radial stress at hub edge B (opposite side of the insertion hub edge) is significantly reduced (95%), annulling the stress concentration, and a non-uniform distribution of radial stress is placed at the middle zone of the interface shaft–hub with a progressive stress reduction as the distance from the insertion hub edge is increased.

The stress relieving effect of optimal chamfer hubs appears at both hub edges. Thus, the stress concentration at the insertion hub edge is lower (33%) than the one corresponding to conventional hubs and the stress concentration is annulled at the opposite side of the hub. The size and magnitude of the plastic zone are lower in optimal chamfer hubs than in conventional hubs. Friction in chamfer hub geometries causes plastic strains lower than the ones generated in conventional hubs. As a result, a huge decrease in stress concentrations (62%) at the opposite hub edge appears due to the combined effect of friction and chamfer geometry.

As a consequence of the changes in the radial stress distributions, a loss of contact pressure is produced after the press-fit assembly. This reduction is higher for chamfer hubs due to the significant stress reduction at the opposite hub edge. Anyway, the loss of contact pressure is lower than 15% for common hub geometries (with low radial interferences and medium hub thickness). Consequently, the use of chamfer hubs in press fits is recommended since a significant reduction in the stress concentration is achieved without significantly reducing the contact pressure.

Author Contributions: Conceptualization, M.L. and E.I.; Data curation, M.L. and E.I.; Formal analysis, M.L. and E.I.; Funding acquisition, M.L.; Investigation, M.L., E.I., M.R.-M. and R.G.-M.; Methodology, M.L. and E.I.; Software, M.L. and E.I.; Supervision, M.L., M.R.-M. and R.G.-M.; Validation, M.L.; Writing—original draft preparation, M.L. and E.I.; Writing—review and editing, M.L., E.I., M.R.-M. and R.G.-M. All authors have read and agreed to the published version of the manuscript.

Funding: This research was funded by the Fundación Memoria D. Samuel Solorzano Barruso, grant numbers FS/32–2017 and FS/12–2021, and by MCIN/AEI/10.13039/501100011033, grant number PID2020–119003GB–I00.

Conflicts of Interest: The authors declare no conflict of interest.

References

1. Chu, S.J.; Jeong, T.K.; Jung, E.H. Effect of radial interference on torque capacity of press-and shrink-fit gears. *Int. J. Automot. Technol.* **2016**, *17*, 763–768. [[CrossRef](#)]
2. Tsai, J.-C.; Chou, T.-T.; Chang, C.-K. Statistical Analysis of Contact Stiffness for Shaft-Bearing Assembly with Tolerancing and Fit. *Procedia CIRP* **2020**, *92*, 45–50. [[CrossRef](#)]
3. Zdravecká, E.; Ondáč, M.; Tkáčová, J.; Vojtko, M.; Slota, J. Failure analysis of the pulleys during the press-fit assembling process. *Case Stud. Eng. Fail. Anal.* **2015**, *3*, 34–38. [[CrossRef](#)]
4. Shu, Y.; Yang, G.; Liu, Z. Experimental study on fretting damage in the interference fit area of high-speed train wheels and axles based on specimen. *Eng. Fail. Anal.* **2022**, *141*, 106619. [[CrossRef](#)]
5. Wang, X.; Lou, Z.; Wang, X.; Xu, C. A new analytical method for press-fit curve prediction of interference fitting parts. *J. Mater. Process. Technol.* **2017**, *250*, 16–24. [[CrossRef](#)]
6. Shigley, J.E.; Mischke, C.R. *Standard Handbook of Machine Design*, 11th ed.; McGraw Hill: New York, NY, USA, 1988.
7. Norton, R.L. *Machine Design*, 5th ed.; Prentice Hall: New York, NY, USA, 2013.
8. Persson, B.N.J. Influence of Surface Roughness on Press Fits. *Tribol. Lett.* **2023**, *71*, 19. [[CrossRef](#)]
9. Calvo, R.; D'Ámato, R.; Gómez, E.; Ruggiero, A. Experimental analysis of the surface roughness in the coefficient of friction test. *Procedia Manuf.* **2019**, *41*, 153–160. [[CrossRef](#)]
10. Wang, T.; Guo, H.; Qiao, J.; Liu, X.; Fan, Z. Experimental study on the relationship between the friction coefficient and interference in locomotive axle press-fitting. *Int. J. Struct. Integr.* **2021**, *12*, 878–893. [[CrossRef](#)]
11. Svahn, F.; Kassman-Rudolphi, Å.; Wallén, E. The influence of surface roughness on friction and wear of machine element coatings. *Wear* **2003**, *254*, 1092–1098. [[CrossRef](#)]
12. Parsons, B.; Wilson, E.A. A method for determining the surface contact stresses resulting from interference fits. *J. Eng. Ind.* **1970**, *92*, 208–218. [[CrossRef](#)]
13. Prasad, N.S.; Sashikanth, P.; Ramamurti, V. Stress distribution in interference joints. *Comput. Struct.* **1994**, *51*, 535–540. [[CrossRef](#)]
14. Arslan, E.; Mack, W. Shrink fit with solid inclusion and functionally graded hub. *Compos. Struct.* **2015**, *121*, 217–224. [[CrossRef](#)]
15. Falter, J.; Binz, H.; Kreimeyer, M. Investigations on design limits and improved material utilization of press-fit connections using elastic-plastic design. *Appl. Eng. Sci.* **2023**, *13*, 100124. [[CrossRef](#)]
16. Güven, U. Stress distribution in shrink fit with elastic-plastic hub exhibiting variable thickness. *Int. J. Mech. Sci.* **1993**, *35*, 39–46. [[CrossRef](#)]
17. Hao, D.; Wang, D. Finite-element modeling of the failure of interference-fit planet carrier and shaft assembly. *Eng. Fail. Anal.* **2013**, *33*, 184–196. [[CrossRef](#)]

18. Lanoue, F.; Vadean, A.; Sanschagrín, B. Finite element analysis and contact modelling considerations of interference fits for fretting fatigue strength calculations. *Simul. Model. Pract. Theory* **2009**, *17*, 1587–1602. [[CrossRef](#)]
19. Zou, L.; Lu, L.; Li, Y.; Yang, K.; Zhao, H.; Dong, Y.; Zeng, D. Experimental and numerical study on press-fitted railway axles: Fretting fatigue behaviour in the very high cycle regime. *Int. J. Fatigue* **2023**, *166*, 107243. [[CrossRef](#)]
20. Shu, Y.; Liu, Z.; Yang, G. Finite element simulation of fretting wear on railway axle press-fit specimens. *Tribol. Int.* **2023**, *178*, 108024. [[CrossRef](#)]
21. Shu, Y.; Yang, G.; Liu, Z. Simulation research on fretting wear of train axles with interference fit based on press-fitted specimen. *Wear* **2023**, *523*, 204777. [[CrossRef](#)]
22. Zou, L.; Zeng, D.; Dong, Y.; Li, J.; Chen, X.; Zhao, H.; Lu, L. Experimental and numerical study on the fretting wear-fatigue interaction evolution in press-fitted axles. *Int. J. Fatigue* **2023**, *175*, 107793. [[CrossRef](#)]
23. Zhang, Y.B.; Lu, L.T.; Zou, L.; Zeng, D.F.; Zhang, J.W. Finite element simulation of the influence of fretting wear on fretting crack initiation in press-fitted shaft under rotating bending. *Wear* **2018**, *400–401*, 177–183. [[CrossRef](#)]
24. Lee, D.H.; Choi, H.Y.; Song, C.Y.; Lee, B.G. Design of stress relief groove on a press-fitted assembly. *Adv. Mater. Res.* **2013**, *753–755*, 1339–1342. [[CrossRef](#)]
25. Lorenzo, M.; Blanco, C.; Moreno, P.; Pérez-Cerdán, J.C. Influence of geometry on the stress peaks in interference fits with grooved hub. *Dyna* **2016**, *91*, 47–51. [[CrossRef](#)]
26. Izard, E.; García-Martín, R.; Rodríguez-Martín, M.; Lorenzo, M. Finite Element Analysis of the Influence of Chamfer Hub Geometry on the Stress Concentrations of Shrink Fits. *Appl. Sci.* **2023**, *13*, 3606. [[CrossRef](#)]
27. Pedersen, N.L. On optimization of interference fit assembly. *Struct. Multidiscip. Optim.* **2016**, *54*, 349–359. [[CrossRef](#)]
28. Izard, E.; García, R.; Rodríguez-Martín, M.; Lorenzo, M. Finite Element Analysis of the Reduction in Stress Concentration Factors in Shrink Fits by Using Contact Rings. *Appl. Sci.* **2022**, *12*, 10037. [[CrossRef](#)]
29. Apatay, T.; Arslan, E.; Mack, W. Effects of homogeneous and inhomogeneous heating on rotating shrink fits with annular inclusion and functionally graded hub. *J. Therm. Stress.* **2019**, *42*, 1458–1479. [[CrossRef](#)]
30. Wang, C.P.; Qi, H.Y.; Hao, W.X.; Hou, D.M. Three-dimensional contact surface modeling and stress analysis of interference fit based on cylindricity error. *Arch. Appl. Mech.* **2022**, *92*, 993–1014. [[CrossRef](#)]
31. Wang, X.; Lou, Z.; Wang, X.; Hao, X.; Wang, Y. Prediction of stress distribution in press-fit process of interference fit with a new theoretical model. *Proc. Inst. Mech. Eng. C J. Mech. Eng. Sci.* **2019**, *233*, 2834–2846. [[CrossRef](#)]
32. Campos, U.A.; Hall, D.E. Simplified Lamé's equations to determine contact pressure and hoop stress in thin-walled press-fits. *Thin Wall. Struct.* **2019**, *138*, 199–207. [[CrossRef](#)]
33. ISO 286-1:2010; Geometrical Product Specifications (GPS)—ISO Code System for Tolerances on Linear Sizes—Part 1: Basis of Tolerances, Deviations and Fits. International Organization for Standardization: Geneva, Switzerland, 2010; p. 38.

Disclaimer/Publisher's Note: The statements, opinions and data contained in all publications are solely those of the individual author(s) and contributor(s) and not of MDPI and/or the editor(s). MDPI and/or the editor(s) disclaim responsibility for any injury to people or property resulting from any ideas, methods, instructions or products referred to in the content.